Wireless Communication Techniques for Improved Detection Fidelity in Microfluidic Impedance Cytometry Using Space–Time Coded Electrodes

Muhammad Tayyab and Mehdi Javanmard

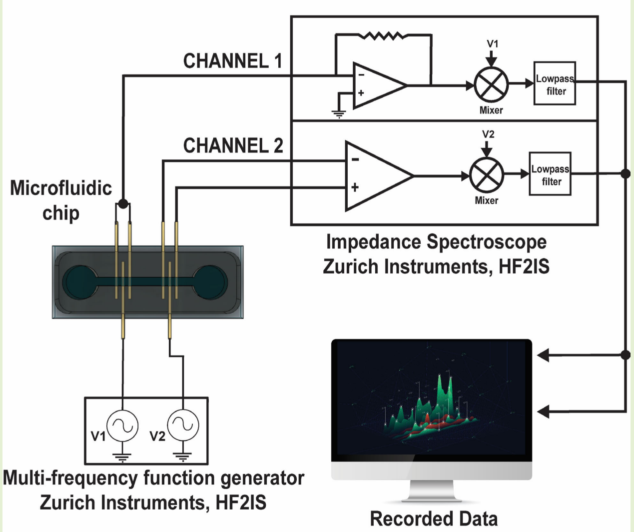

***Abstract*—Microfluidic flow cytometry may be used to provide important knowledge about the characteristics of microparticles, including cell size, intracellular organelles, and DNA damage response. Since there is so much study in this field, several strategies have been used to improve the system's effectiveness in a variety of areas, including sample preparation, sensing modalities, and data analysis. Due to the simplicity with which electrical components may be downsized, reduced cost, portability, and simplicity of the system, impedance-based detection offers an inherent benefit over various sensing modalities. Although electrical-based cytometry systems have a number of benefits over their optical equivalents, some problems still need to be resolved before standalone point-of-care (POC) solutions can be achieved. False peak counts caused by spurious interference, which can taint the accurate cytometry counts, are one of the key issues with electrical-based systems. In this article, we introduce a novel algorithm for error correction employing space–time coded electrodes as a first step toward a viable solution. Using our novel symbol-combining approach, we are able to increase the signal detection fidelity through an improvement in the signal-to-noise ratio (SNR) of three times compared to simple thresholding. Based on the increased SNR, we present a smart thresholding technique to increase signal fidelity and reduce the effects of spurious peaks and noise.**

***Index Terms*— Biosensors, impedance spectroscopy, space–time coding, wireless communications.**

I. Introduction

MICROFLUIDICS is the study and manipulation of small volumes of fluid, generally in the order of microliters to nanoliters through the use of microfluidic devices comprising channels with dimensions in the micrometer and nanometer range [1]. Microfluidics has emerged as a field with wide-ranging applications in diverse and broad fields such as biology [2], medicine [3], diagnostics [4], and environmental science [5], to name a few. Perhaps, the most important and widely researched application of microfluidics is microfluidic flow cytometry [6]. In flow cytometry, microparticles or cells have flowed through a device where these particles are hydrodynamically focused to a sensing region [7]. Microfluidic flow cytometry can provide valuable insights into the properties of microparticles such as size of cells [8], intracellular organelles [9], and DNA damage response [10]. Since this is such a wide area of research, numerous approaches have been adopted to increase the efficiency of the system on various fronts such as sample preparation [11], sensing modalities [12], and data analysis [13].

Received 18 August 2024; revised 9 November 2024; accepted 11 November 2024. Date of publication 4 December 2024; date of current version 14 January 2025. This work was supported by the National Science Foundation CAREER under Award 1556253. The associate editor coordinating the review of this article and approving it for publication was Prof. Shakeb A Khan. *(Corresponding author: Muhammad Tayyab.)*

The authors are with Rutgers, The State University of New Jersey, Piscataway, NJ 08901 USA (e-mail: mt1013@scarletmail.rutgers.edu; mehdi.javanmard@rutgers.edu).

Digital Object Identifier 10.1109/JSEN.2024.3506697

1558-1748 © 2024 IEEE. Personal use is permitted, but republication/redistribution requires IEEE permission.
See https://www.ieee.org/publications/rights/index.html for more information.

Authorized licensed use limited to: Rutgers University Libraries. Downloaded on May 20,2025 at 20:38:08 UTC from IEEE Xplore. Restrictions apply.

Various sensing modalities have been studied for microfluidic flow cytometry. Of these, the most common one is optical flow cytometry. An optical flow cytometer comprises basically fluidics, optics (excitation and collection), an electronic network (detectors), and a computer [14]. Optical flow cytometers have the ability to detect multiple parameters accurately and have been used for the advancement of cellular biology and diagnostic applications [15], [16]. Despite having numerous advantages, optical flow cytometers have some limitations when using these in a resource-limited setting. First, optical flow cytometers are prohibitively expensive and require expensive reagents for optically labeling cells [17]. Furthermore, flow cytometers are not easy to operate and require multiple sample preparation steps, which increase the fluid handling complexity and require skilled expertise for use. Recently, there has been a push for miniaturization of the optical flow cytometer in an effort to combat the challenges associated with their use in a limited resource setting to realize a point-of-care solution [18], [19]. Furthermore, there are other novel approaches such as using smartphones for cell counting and sorting, which use the camera sensors present in the smartphone in an effort to make cell counting and microparticle imaging more accessible [20], [21]. Although these efforts are commendable, smartphone-based imaging requires a smartphone with an acceptable level of camera resolution, and most of the developed approaches work with a limited number of smartphones. Furthermore, the use of fluorescent reagents and off-chip sample preparation required presents the problems already discussed for the conventional flow cytometers.

While microfluidic technology reduces the size of fluidic components, entire systems with peripherals remain too large and costly for point-of-care (POC) use, often requiring professional alignment and troubleshooting [22]. Wallace H. Coulter is known to have invented the first commercial impedance-based particle counter known as the Coulter counter first sold in 1956, which, interestingly, operates on the Coulter principle [23]. According to the Coulter principle, individual cells are made to travel via a narrow, constrained electric current route in the suspending fluid, and detection is based on variations in the electrical conductivity of the cell and the suspending fluid [24]. This sparked interest in a whole new industry revolving around microfluidic impedance cytometry.

Since the invention of the first Coulter counter in the mid-1950s, microfluidic impedance cytometers have seen improvement on many fronts and have been used for the classification of cells [25] for the detection of proteins [26], nucleic acids [27], and even cancer biomarkers [28]. Impedance-based detection offers an inherent advantage due to the ease with which electrical components can be miniaturized, thereby reducing cost and making the system portable and easy to use [4], [29], [30], [31]. Although electrical-based cytometry systems offer various advantages over their optical counterparts, there are certain challenges that remain to be solved in order to realize stand-alone POC solutions. One of the main challenges associated with electrical-based systems is false peak counts resulting from spurious interference, which can corrupt the correct cytometry counts [32]. Attempts have been made to resolve this by employing digital signal processing methods to remove noise and for signal recovery [33].

Thresholding remains a challenge; at what point does a "peak-like signature" in impedance cytometry representing the microparticle of interest flowing through the sensing region become spurious noise due to electrical interference? One way to answer this question, which has already been done by a few researchers, is to image the flow of particles as they move through the electrical sensing region and record optical data simultaneously to cross-verify the passing of the desired microparticle with the recorded electrical peak signature [34], [35], [36]. However, such a method is costly, requires additional circuitry and equipment for its implementation, and, thus, diminishes the value of using impedance-based methods in the first place, which offer inherent cost reduction and easier implementation in the first place.

Various signal enhancement techniques have been applied to enhance signal fidelity. One such method is to alter the electrical characteristics of the analyte to generate a specific electrical signature [37]. The drawback of such a method is the added complexity of sample preparation and incurring high costs. Researchers have also explored the use of machine learning (ML) and artificial intelligence (AI) to enhance detection fidelity [27], [38]. These methods require high computational power for their use and may present challenges to implement in resource-constrained settings.

In this article, we present a step in the direction of a potential solution through the implementation of a novel algorithm for error correction using space–time coded electrodes. Our method draws inspiration from an advanced wireless communication technique that was presented by Alamouti [31] for the development of a simple transmit diversity technique utilizing multiple antennas for increasing the signal quality in wireless communication systems. The purpose of this article is to apply the wireless communication techniques to microfluidic impedance cytometry; however, readers interested in reviewing these concepts in more detail may wish to refer to the existing literature surrounding the topic [39], [40], [41]. Here, we give a brief background of the original communication technique by Alamouti in this article and explain how we designed and developed our microfluidic chip with integrated space–time coded electrodes. We demonstrate how the space–time coded electrodes coupled with our signal combination algorithm can be used for increasing fidelity in microfluidic cytometry and establishing a more accurate cytometer count with enhanced fidelity. Finally, we discuss the potential future applications of the novel technique and how it can be improved to be implemented for further use.

II. SPACE–TIME CODING ALGORITHM

A. Alamouti Code

The Alamouti code is a popular wireless transmission scheme that provided the basis of many multiple-input–multiple-output (MIMO) systems. We provide a brief description of the Alamouti code in this section. For a full explanation of the algorithm in detail, the reader is encouraged to refer

Authorized licensed use limited to: Rutgers University Libraries. Downloaded on May 20,2025 at 20:38:08 UTC from IEEE Xplore. Restrictions apply.

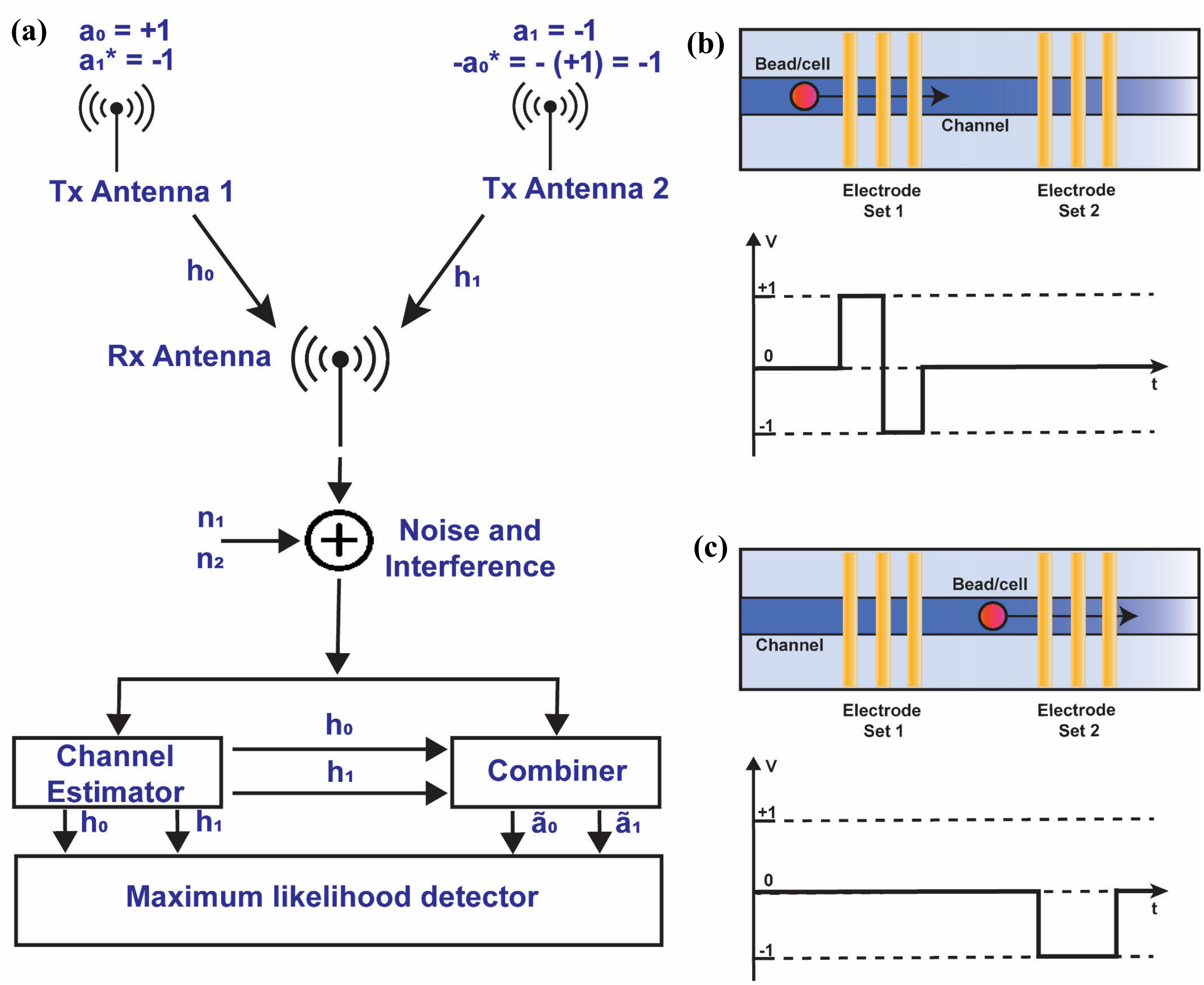

Fig. 1. Development of the space–time coded algorithm encoding sequence. (a) Original Alamouti code encoding sequence and combining scheme simplified block diagram. Adapted from [31]. (b) Encoding sequence for electrode set 1. The signature signal produced when a bead or a microparticle passes through the electrode set 1. (c) Encoding sequence for electrode set 2. The signature signal produced when a bead or a microparticle passes through the electrode set 2.

to the original publication [31]. It is used to increase the quality of the signal in wireless communication systems by making use of multiple antennas to achieve transmit diversity. It is a very popular scheme from a practical implementation point of view since the channel information is not needed at the transmitter for reliable wireless communication. The basic implementation of an Alamouti code is shown in Fig. 1(a). It is a straightforward transmit diversity system that enhances the quality of the signal at the receiver on one end of the link by straightforward processing across two transmit antennas on the other end. This transmit diversity technique can increase the wireless communications systems' capacity, data rate, and error performance. It may be possible to utilize higher level modulation methods to raise the effective data rate or smaller reuse factors in a multicell environment to boost system capacity due to the decreased sensitivity to fading. One of the major advantages of using this scheme is that it combats multichannel fading without the need for prior knowledge about the channel at the receiver end.

A brief description of the Alamouti code is presented here, which is adapted from the original publication by Alamouti [31]. For a full explanation of the algorithm in detail, the reader is encouraged to refer to the original publication. The algorithm is defined by three functions: the encoding and transmission sequence at the transmitter, the combining scheme at the receiver, and the decision rule for maximum likelihood detection. We will first discuss the encoding scheme and how we use this encoding scheme for the design of our space–time block coded electrodes in a microfluidic chip. In the original proposed scheme, two signals are simultaneously transmitted from the two transmit antennas shown in Fig. 1(a). The symbol transmitted by one antenna is denoted as $\mathbf{a_0}$, and the signal transmitted by the other antenna is denoted as $\mathbf{a_1}$. Now, during the next symbol period, $(-\mathbf{a}_1^*)$ is transmitted from the first antenna and the symbol $\mathbf{a}_0^*$ is transmitted from the second antenna.

Thus, at time $\mathbf{t_0}$, the two antennas transmit the first sequence. At time $\mathbf{t_1} = \mathbf{t_0} + \mathbf{\Delta t}$, the two antennas transmit the second sequence, where $\mathbf{\Delta t}$ is the time between the two transmissions. The fading across the two symbols is assumed to be constant i.e.,

$$\begin{aligned} h_0(t_0) &= h_0(t_0 + \Delta t) \\ h_1(t_0) &= h_1(t_0 + \Delta t). \end{aligned} \tag{1}$$

Authorized licensed use limited to: Rutgers University Libraries. Downloaded on May 20,2025 at 20:38:08 UTC from IEEE Xplore. Restrictions apply.

The received signals can then be represented as $\mathbf{r_0}$ and $\mathbf{r_1}$

$$\begin{aligned} r_0 &= r(t) = h_0 a_0 + h_1 a_1 + n_0 \\ r_1 &= r(t_0 + \Delta t) = -h_0 a_0^* + h_1 a_1^* + n_1 \end{aligned} \tag{2}$$

where $\mathbf{n_0}$ and $\mathbf{n_1}$ are the complex variables representing receiver noise. The combining scheme is rather straightforward and is one of the main reasons why the Alamouti code is attractive in terms of implementation complexity.

B. Space–Time Coded Electrodes for Microfluidic Impedance Cytometry

The two antennas can be represented as two electrode pairs forming an electrode set. We can configure the electrodes in such a way that they follow an encoding sequence similar to that of the Alamouti code in a binary phase shift keying (BPSK) format when a bead passes through the sensing region. Fig. 1(b) demonstrates the two electrode pairs analogous to the two antennas and has two sets of separated electrodes for the transmission of the encoding sequence. When a bead passes through the electrode set, a signature signal is produced, which can be seen in the figure. The bead will then pass through the second electrode set, which consists of two electrode pair system again, and will give rise to a signature peak signal, as demonstrated in Fig. 1(c). The distance between the two electrode pairs will define the time between the transmissions of the symbol pairs analogous to $\mathbf{\Delta t}$. The benefit of using this electrode configuration and the encoding scheme is that we can later use the combining scheme to increase the fidelity of detection and classify a peak as a true peak only if the combining scheme yields a high signal i.e., if both the peak signatures from the electrode sets are present. This leads to increased confidence in the choice of classifying a peak as a bead/microparticle passing through instead of having an estimate of the threshold based on empirical and theoretical analysis alone.

The combining scheme in the traditional Alamouti code is usually done using a combiner [see Fig. 1(a)], which combines the signals in the following manner to yield $\mathbf{\tilde{a}_0}$ and $\mathbf{\tilde{a}_1}$:

$$\begin{aligned} \tilde{a}_0 &= h_0^* r_0 + h_1 r_1^* \\ \tilde{a}_1 &= h_1^* r_0 - h_0 r_1^*. \end{aligned} \tag{3}$$

In the case of a microfluidic channel, we can have the simple assumption that the fading across both electrode sets is similar. Therefore, $\mathbf{h_1} = \mathbf{h_2}$, which, in a physical sense, translates to the channel's electrical properties being the same across both electrode pairs. This greatly simplifies the combining scheme, and we can simply take the difference of the signal for the first two received symbols and take the sum of the second two symbols to get the received symbol. In the case of microfluidic impedance cytometry, we only have two types of symbols i.e., either there is a bead passing through the electrodes or there is not. Therefore, this is similar to BPSK signals, and the decision rule for the maximum likelihood detection for the simple case can then be used

choose $\mathrm{a_i}$ iff

$$d^2(\tilde{a}_0, a_i) \leq d^2(\tilde{a}_0, a_k) \quad \forall i \neq k. \tag{4}$$

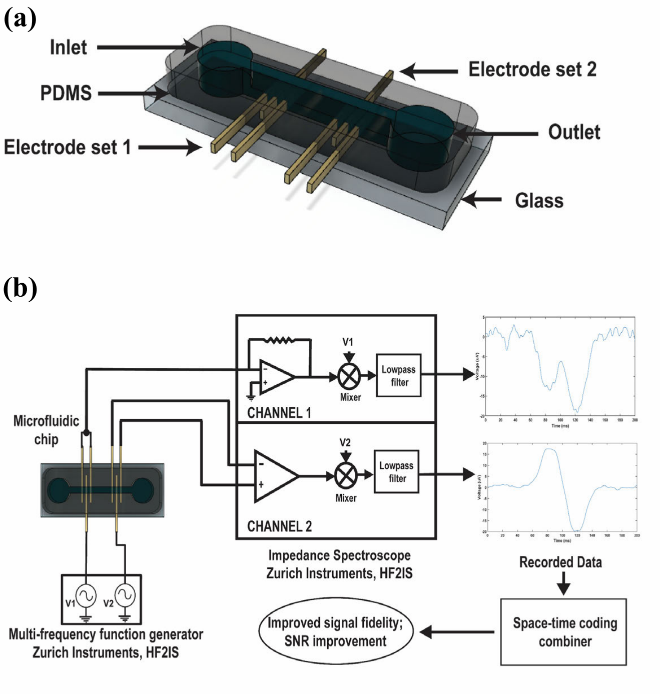

Fig. 2. Microfluidic system electrode configuration overview. (a) Schematic of the microfluidic chip with the space–time coded gold electrodes. (b) System block diagram. One set of electrodes is connected to the single-ended measurement channel (channel 1), whereas the other set of electrodes is connected to the differential signal demodulator (channel 2).

The implication of this decision rule in microfluidic impedance cytometry is that we should choose the symbol, which is closest to the received signal after it has passed through the combiner. We will see in Sections III-A and III-B how this is done by considering a practical scenario.

C. Experimental Setup

A 3-D schematic of the microfluidic chip can be seen in Fig. 2(a). The chip comprises two gold electrode sets patterned onto a glass wafer with a polydimethylsiloxane (PDMS) channel overlayed on top of the electrodes; 2.8-μm microbeads (Dynabeads[1] M-280 Tosylactivated) were used for the purpose of our experiments. The beads are pipetted into the inlet and are allowed to flow under the capillary flow from the inlet to the outlet. Fig. 2(b) provides a system block diagram of the electronic impedance measurement setup using a benchtop impedance spectroscope. The electrical data are captured using the commercial HF2IS benchtop impedance spectroscope from Zurich Instruments. The data are recorded for approximately 10 min. The commercial benchtop impedance spectroscope's electrical parameters can be programmed according to the user's requirements. The commercial benchtop instrument provides two channels for the impedance measurement. The middle electrode in both the electrode sets is connected to the output of the benchtop instrument, which acts as a function generator providing the necessary excitation signal for the measurement. We use 1 V as the excitation voltage for both

---

[1] Trademarked.

Authorized licensed use limited to: Rutgers University Libraries. Downloaded on May 20,2025 at 20:38:08 UTC from IEEE Xplore. Restrictions apply.

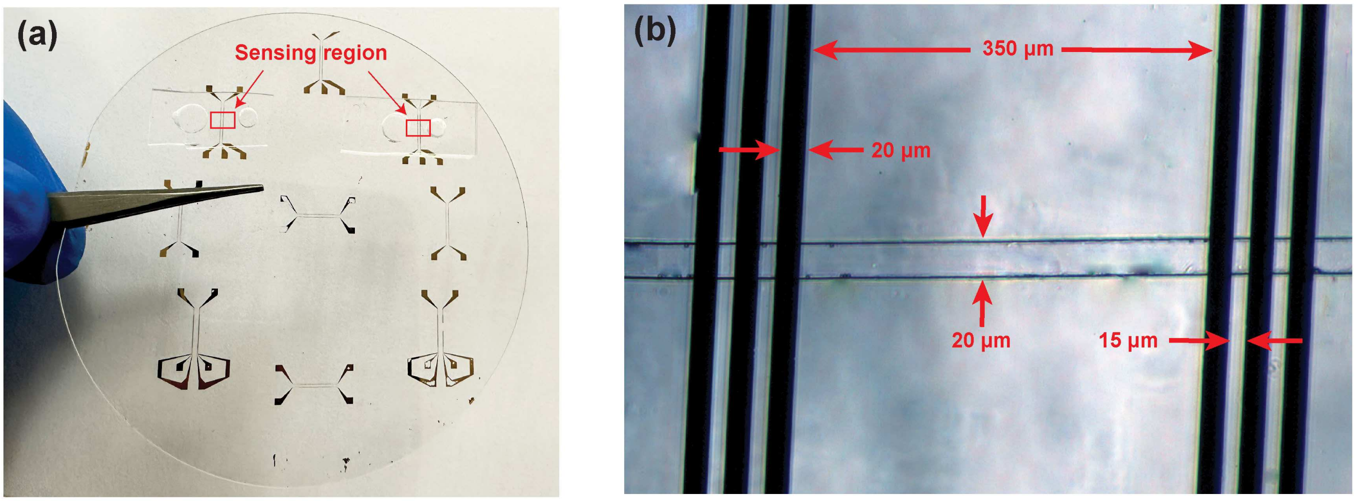

Fig. 3. Microfluidic chip with integrated space–time coded gold electrodes. (a) Photograph of the fabricated microfluidic chip with the integrated gold electrodes. (b) Microscopic image of the fabricated microfluidic chip with gold electrodes and the PDMS channel. The channel is 20 μm in width and 15 μm in height. The gold electrodes are 100 nm thick.

the electrode sets and use a frequency of 500 kHz. The other two electrodes for electrode set 1 are connected together and passed through a commercial transimpedance amplifier (Zurich Instruments, HF2TA). The transimpedance gain of the amplifier can be programmed through the graphical user interface of the instrument. A transimpedance gain of 1 kV/A was chosen for the purposes of our experiment. This signal is then fed into the input of channel 1 of the instrument, which is configured for single-ended measurements. The demodulation of the signal occurs digitally via the impedance spectroscope, where it is mixed with the original signal and a low pass filter is applied to the signal to reduce the spurious noise beyond the required bandwidth. The bandwidth of the impedance spectroscope can also be tuned through software, and it was set to be equal to 100 Hz. This implies that the signal would be filtered to exclude any particle crossing the sensing zone faster than 10 ms or any change in impedance occurring faster than 10 ms, such as jitter. The second set of electrodes is fed into the input of channel 2 of the impedance spectroscope, which is configured for differential-ended signals. This is demodulated after passing through a differential amplifier, and the signal is demodulated in the same manner by a mixer and a low-pass filter. Finally, the data are recorded on a personal computer and are processed using the custom algorithm for achieving increased detection fidelity and smart thresholding.

D. Microfluidic Chip Fabrication

The microfluidic chip is made of PDMS and has embedded gold electrodes on a glass surface. The first step in making the microfluidic chip is to pattern and make the electrodes on the glass wafer. Traditional photolithography is used to create electrodes on glass using a 3″ fused silica wafer. The technique includes the following steps: photo-patterning resist on the fused silica wafer, liftoff processing, and electron beam metal evaporation. The photo-patterning procedure includes washing the wafers, spin coating the photoresist, soft baking the resist, exposing the resist to ultraviolet light through a chromium mask printed on a 4 × 4 glass plate, developing the resist, and hard baking the resist. An electron beam evaporation approach deposits a 100-nm-thick layer after photograph patterning. A 10-nm coating of chromium is used to improve the gold's adhesion to the glass wafer because, without it, the gold film is easily ripped off. Gold was chosen as the electrode because of its inertness and corrosion resistance. With a 15-μm space between each electrode, the electrodes were each 20-μm broad in each electrode set. The two electrode sets are 350 μm apart in length.

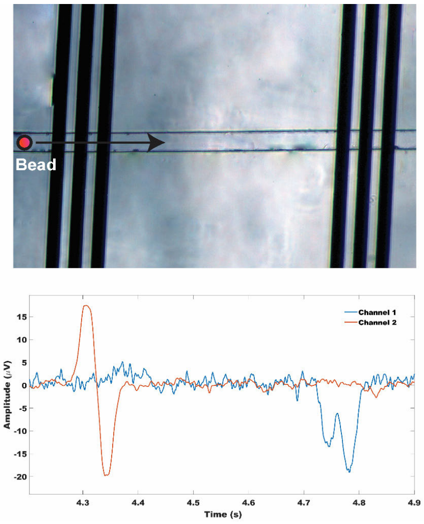

Fig. 4. Recorded signal response. The recorded signal response for both the channels of the impedance spectroscope is displayed (bottom) representing a signal when a bead may be passing through the electrode sets as shown (top).

A photograph of the fabricated microfluidic chip can be seen in Fig. 3(a). We fabricated the microfluidic channel in PDMS using soft lithography. A layer of SU-8 was printed on a 3″ silicon wafer that acts as a primary mold. The SU-8 photo-patterning procedure includes the phases of standard cleaning, spin coating, soft baking, exposure, development,

Authorized licensed use limited to: Rutgers University Libraries. Downloaded on May 20,2025 at 20:38:08 UTC from IEEE Xplore. Restrictions apply.

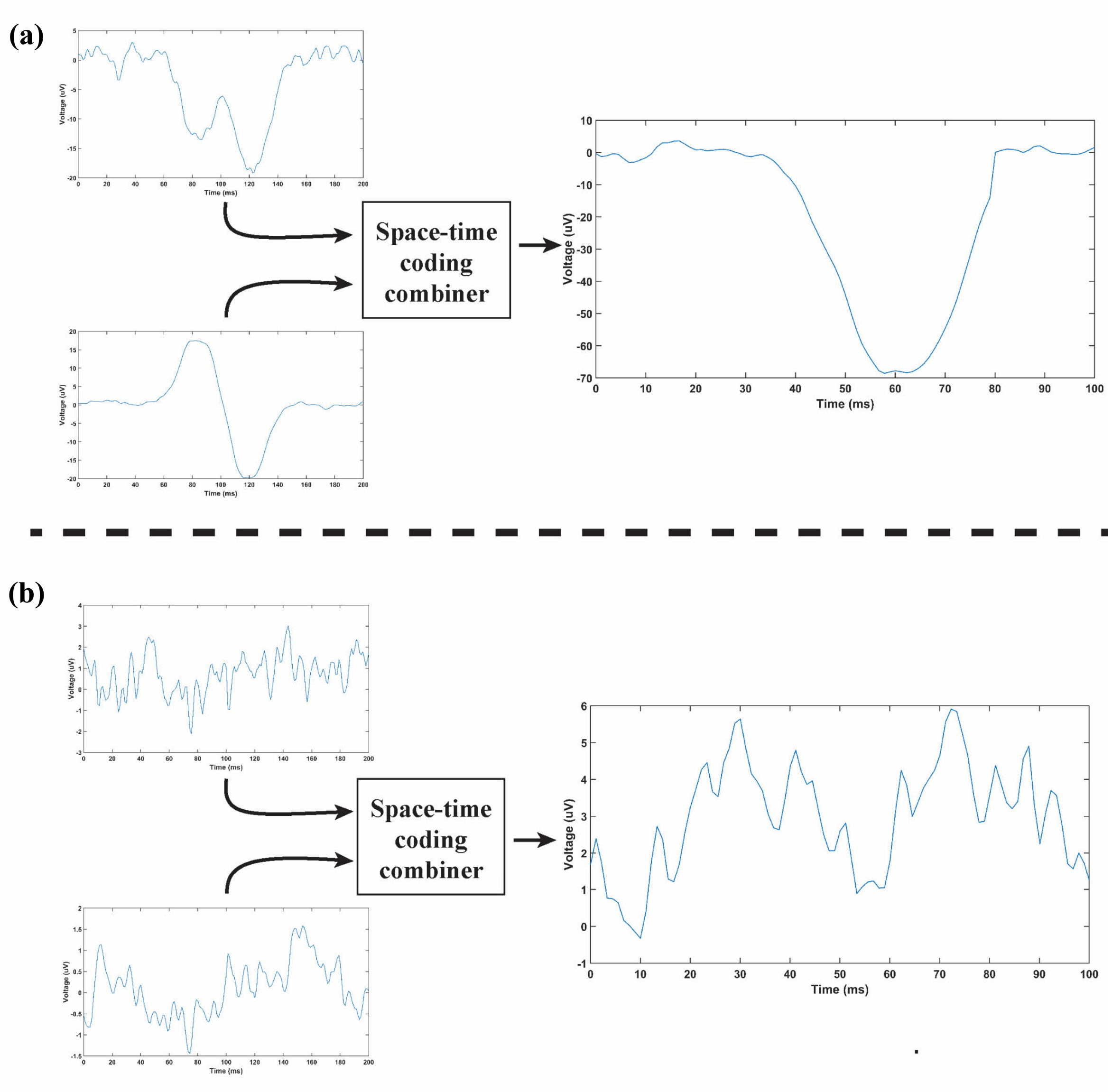

Fig. 5. Illustration of the space–time coding combiner scheme. (a) Space–time coding combiner scheme is demonstrated on a peak with a significant amplitude compared to the noise. The combining scheme results in a single peak roughly four times the amplitude of the original peak. (b) Space–time coding combiner scheme is demonstrated when two noise segments are combined using the combining scheme. As we can see, the signal is not amplified in this case, and the noise remains somewhat similar to the original inputs from channels 1 and 2.

and hard baking. After the primary mold was made, it was coated with PDMS (10:1 prepolymer/curing agent), which was then baked at 80 °C for 2 h to cure it. After that, the PDMS channel was taken out of the mold. After that, two holes were punched, one measuring 5 mm and the other 3 mm, to provide the outflow and entrance. The PDMS substrate was then put in place and attached to the electrode chip after both substrates had received oxygen plasma treatment. The chip was then baked for 40 min at 70 °C to form the irreversible bond. Our microfluidic tube had dimensions of 20 μm wide and 15 μm tall. A microscopic image of the sensing region can be seen in Fig. 3(b).

III. RESULTS

In a simple two-electrode microfluidic cytometry format, as a bead passes through the sensing region between the electrodes, a signal is generated. This signal is generated due to a change in the impedance between the two electrodes and is in the form of a single peak in the voltage response. This negative peak represents a sudden rise in the impedance and can be construed as a bead or cell passing through the electrodes. However, there is a problem with determining the threshold of such a system. Here, we present a solution for better detection fidelity using space–time coded electrodes. As a bead passes through the first set of the space–time coded electrodes, it presents a signal similar to the $[1\ -1]$ pattern seen in Fig. 1(b). Similarly, a signal representing the $[-1\ -1]$ pattern is seen when the bead or cell passes through the second set of the space–time coded electrodes. The result of a bead passing through can be seen in Fig. 4. Channel 1 of the impedance spectroscope is connected to the electrode set 2, which generates the $[-1\ -1]$ peak signature, and

Authorized licensed use limited to: Rutgers University Libraries. Downloaded on May 20,2025 at 20:38:08 UTC from IEEE Xplore. Restrictions apply.

channel 2 is connected to the electrode set 1, which generates the $[1\ -1]$ peak signature. The differential signal channel has higher amplification, and to apply the combination algorithm successfully, it is scaled by a factor of 1/6.

A. Space–Time Coding Combining Scheme

The combining scheme for the space–time coded electrodes draws inspiration from the original Alamouti code. In this combining scheme, we take the two symbols that are being transmitted via the two electrode sets and combine them in a way that they interfere constructively.

Consider the two ideal symbols from electrode set 1: $[-1\ -1]$ and the two symbols from electrode set 2: $[1\ -1]$. To interfere constructively, we can take the difference between the first two symbols and the sum of the second two symbols. This will yield a result: $[-2\ -2]$. Now, we apply a successive combination of the two symbols since, in the case of microfluidic impedance cytometry, both these symbols either represent the passing of a bead or spurious noise. The successive combination is a summation of the two symbols, which will yield $[-4]$.

The main idea behind this combination scheme is that the true peaks, which are the ones generated by an actual bead or a cell passing through, will have an enhanced signal, whereas the noise or spurious peaks will not. This concept is shown for a peak recorded for beads passing through the channel in Fig. 5(a). As we can see from this figure, the four recorded symbols suffer from nonuniform fading and have slightly different peak amplitudes between 15 and 20 μV. After applying the custom space–time coded combining scheme, we can see that the amplitude of the peak is approximately four times the original amplitude. This is in line with our theory that a true peak will interfere constructively to give a strong signal. The application of the combination scheme on noise, however, yields a different result. This can be seen in Fig. 5(b). We can see that the noise in the system is not nearly as amplified, if at all. This is in line with our theory that the noise will not be amplified and only the signal can be enhanced.

B. SNR Improvement

We now take a look at the improvement in signal detection accuracy in terms of a quantifiable quantity, the signal-to-noise ratio (SNR). For this purpose, we use simple peak detection using a threshold level in an experiment where we set the threshold value to 13 μV. A total of 216 peaks were detected in this experiment. We apply the space–time coding combining algorithm and look at the increase in the signal level for the peaks. We also inspect the noise associated with the peaks when applying the space–time code combining algorithm and analyze the average noise amplitude for both noise and the peaks. The results of this analysis are shown in Fig. 6(a). We can see that the SNR for the case with simple thresholding is

$$\text{SNR (Simple peak detection)} = \frac{\text{Average peak amplitude}\ \ (\mu\text{V})}{\text{Average noise amplitude}\ \ (\mu\text{V})} = \frac{18.92}{7.87} = 2.4 \qquad (5)$$

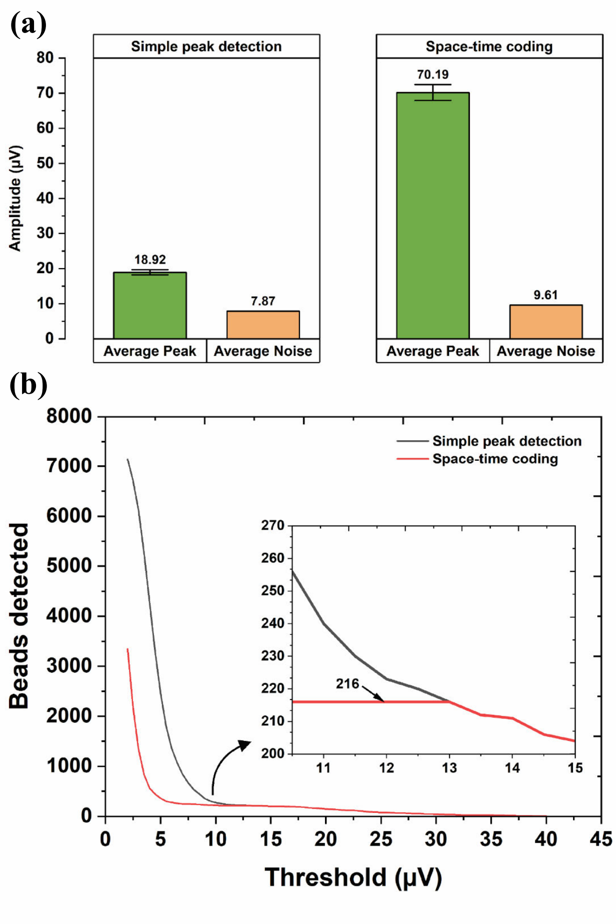

Fig. 6. Quantitative analysis of the improved detection fidelity using space–time coded electrodes and combining scheme. (a) Analysis of the signal and noise amplitudes using space–time coded combining scheme compared with simple peak detection and the custom space–time coding combining scheme. (b) Demonstration of smart thresholding applied to an experiment versus the simple peak detection using variable threshold values.

whereas the SNR for the space–time coding can be computed as

$$\text{SNR (Space time coding)} = \frac{\text{Average peak amplitude}\ \ (\mu\text{V})}{\text{Average noise amplitude}\ \ (\mu\text{V})} = \frac{70.19}{9.61} = 7.3. \qquad (6)$$

Therefore, the SNR improvement is $7.3/2.4 \approx 3$, representing at least a three times improvement in the signal detection fidelity.

C. Smart Thresholding—Enhanced Detection Fidelity

As we can see, there is an SNR improvement when applying the space–time coding combining scheme on the detected peaks, whereas there is no significant improvement in terms of signal amplitude when applying it to noise. We can leverage this property of the combining scheme to come up with a smart thresholding algorithm, where we can only quantify the peaks as a true peak if there is a signal enhancement when combining the received symbols from the two electrode sets. This will separate the noise and the spurious peaks

Authorized licensed use limited to: Rutgers University Libraries. Downloaded on May 20,2025 at 20:38:08 UTC from IEEE Xplore. Restrictions apply.

from the true peaks. We can set a criterion similar to the one used in (4) to determine whether the received symbol is closer to the noise or the peak signal. For this reason, we determine that the peak may only be considered a true peak if the combined signal is significantly higher than the originally detected signal, specifically 2.5× higher. We analyze the results of smart thresholding on an experiment with beads. The results of this analysis are shown in Fig. 6(b), where we vary the threshold in increments of 0.5 μV and record the peaks obtained through simple peak detection via thresholding. We then apply the combination algorithm to each of these peaks and determine whether or not each peak undergoes signal amplification due to the combination. As we can see in the figure, the space–time coding combination algorithm yields a near-straight line even as we decrease the threshold, whereas the simple peak detection peaks increase linearly for a period of time and quickly increase exponentially. This exponential increase represents a breakdown of the detection algorithm since the false peaks are now included in the detection count. We can see that the space–time coding algorithm applied to the same data yields a much better count and is a nearly straight line between 7 and 13 μV. Therefore, we can set the threshold in this region, which is much lower than with normal peak detection, and get an accurate count without losing detection accuracy.

IV. CONCLUSION

We have demonstrated that we can increase the detection fidelity by adapting advanced wireless communication techniques and applying them to microfluidic impedance cytometry. In particular, we have demonstrated the application of space–time coded electrodes to achieve increased SNR improvement, as well as providing us with a method for smart thresholding to decrease spurious peaks and noise. The results presented here act as a proof of concept for increasing detection fidelity by performing experiments with biological cells and obtaining a true peak count. The increased performance for the peak detection fidelity will enable us to achieve better results in terms of signal accuracy and confidence without the need for drastically modifying the system architecture of a typical microfluidic impedance cytometer. We have used a benchtop impedance spectroscope in this research. This can be easily replaced by a custom lock-in amplification system such as the ones already presented in the literature to bring us closer to a reliable point-of-care-based microfluidic impedance cytometry solution, thereby enhancing detection fidelity.

REFERENCES

[1] G. M. Whitesides, "The origins and the future of microfluidics," *Nature*, vol. 442, no. 7101, pp. 368–373, Jul. 2006.

[2] M. Javanmard et al., "A microfluidic platform for characterization of protein–protein interactions," *IEEE Sensors J.*, vol. 9, no. 8, pp. 883–891, Aug. 2009.

[3] J. Chen, D. Chen, Y. Xie, T. Yuan, and X. Chen, "Progress of microfluidics for biology and medicine," *Nano-Micro Lett.*, vol. 5, no. 1, pp. 66–80, Mar. 2013.

[4] M. Tayyab et al., "A portable analog front-end system for label-free sensing of proteins using nanowell array impedance sensors," *Sci. Rep.*, vol. 12, no. 1, Nov. 2022, Art. no. 20119.

[5] A. Gholizadeh, S. Sardar, K. Francisco, A. Maher, R. Miskewitz, and M. Javanmard, "Towards in-situ environmental monitoring: On-chip sample preparation and detection of lead in sediment samples using graphene oxide sensor," *IEEE Sensors J.*, vol. 20, no. 22, pp. 13787–13795, Nov. 2020.

[6] Y. Gong, N. Fan, X. Yang, B. Peng, and H. Jiang, "New advances in microfluidic flow cytometry," *Electrophoresis*, vol. 40, no. 8, pp. 1212–1229, Apr. 2019.

[7] K. A. Muirhead, P. K. Horan, and G. Poste, "Flow cytometry: Present and future," *Biotechnology*, vol. 3, no. 4, pp. 337–356, Apr. 1985.

[8] J. Gray, F. Dolbeare, M. Pallavicini, W. Beisker, and F. Waldman, "Cell cycle analysis using flow cytometry," *Int. J. Radiat. Biol. Rel. Stud. Phys., Chem. Med.*, vol. 49, no. 2, pp. 237–255, 1986.

[9] R. Regmi, K. Mohan, and P. P. Mondal, "High resolution light-sheet based high-throughput imaging cytometry system enables visualization of intra-cellular organelles," *AIP Adv.*, vol. 4, no. 9, Sep. 2014, Art. no. 097125.

[10] Z. Darzynkiewicz, F. Traganos, H. Zhao, H. D. Halicka, J. Skommer, and D. Wlodkowic, "Analysis of individual molecular events of DNA damage response by flow-and image-assisted cytometry," in *Recent Advances in Cytometry, Part B* (Methods in Cell Biology), vol. 103, 2011, pp. 115–147.

[11] J. Petriz, J. A. Bradford, and M. D. Ward, "No lyse no wash flow cytometry for maximizing minimal sample preparation," *Methods*, vols. 134–135, pp. 149–163, Feb. 2018.

[12] J. Woo, A. Baumann, and V. Arguello, "Recent advancements of flow cytometry: New applications in hematology and oncology," *Expert Rev. Mol. Diag.*, vol. 14, no. 1, pp. 67–81, Jan. 2014.

[13] A. Bashashati and R. R. Brinkman, "A survey of flow cytometry data analysis methods," *Adv. Bioinf.*, vol. 2009, pp. 1–19, Dec. 2009.

[14] A. Adan, G. Alizada, Y. Kiraz, Y. Baran, and A. Nalbant, "Flow cytometry: Basic principles and applications," *Crit. Rev. Biotechnol.*, vol. 37, no. 2, pp. 163–176, Feb. 2017.

[15] H. M. Shapiro, "Multistation multiparameter flow cytometry: A critical review and rationale," *Cytometry, J. Int. Soc. Anal. Cytol.*, vol. 3, no. 4, pp. 227–243, Jan. 1983.

[16] M. Tayyab, M. A. Sami, H. Raji, S. Mushnoori, and M. Javanmard, "Potential microfluidic devices for COVID-19 antibody detection at point-of-care (POC): A review," *IEEE Sensors J.*, vol. 21, no. 4, pp. 4007–4017, Feb. 2021.

[17] P. A. Arndt and G. Garratty, "A critical review of published methods for analysis of red cell antigen-antibody reactions by flow cytometry, and approaches for resolving problems with red cell agglutination," *Transfusion Med. Rev.*, vol. 24, no. 3, pp. 172–194, Jul. 2010.

[18] M. Rosenauer, W. Buchegger, I. Finoulst, P. Verhaert, and M. Vellekoop, "Miniaturized flow cytometer with 3D hydrodynamic particle focusing and integrated optical elements applying silicon photodiodes," *Microfluidics Nanofluidics*, vol. 10, no. 4, pp. 761–771, Apr. 2011.

[19] S. M. Bryce, S. L. Avlasevich, J. C. Bemis, S. Phonethepswath, and S. D. Dertinger, "Miniaturized flow cytometric *in vitro* micronucleus assay represents an efficient tool for comprehensively characterizing genotoxicity dose–response relationships," *Mutation Research/Genetic Toxicol. Environ. Mutagenesis*, vol. 703, no. 2, pp. 191–199, Dec. 2010.

[20] M. A. Sami, M. Tayyab, and U. Hassan, "Excitation modalities for enhanced micro and nanoparticle imaging in a smartphone coupled 3D printed fluorescent microscope," *Lab Chip*, vol. 22, no. 19, pp. 3755–3769, 2022.

[21] M. A. Sami, M. Tayyab, P. Parikh, H. Govindaraju, and U. Hassan, "A modular microscopic smartphone attachment for imaging and quantification of multiple fluorescent probes using machine learning," *Analyst*, vol. 146, no. 8, pp. 2531–2541, 2021.

[22] T. D. Chung and H. C. Kim, "Recent advances in miniaturized microfluidic flow cytometry for clinical use," *Electrophoresis*, vol. 28, no. 24, pp. 4511–4520, Dec. 2007.

[23] J. P. Robinson, "Wallace H. Coulter: Decades of invention and discovery," *Cytometry A*, vol. 83A, no. 5, pp. 424–438, May 2013.

[24] M. D. Graham, "The Coulter principle: Foundation of an industry," *Jala, J. Assoc. Lab. Autom.*, vol. 8, no. 6, pp. 72–81, Dec. 2003, doi: 10.1016/s1535-5535-03-00023-6.

[25] H. Raji, M. Tayyab, J. Sui, S. R. Mahmoodi, and M. Javanmard, "Biosensors and machine learning for enhanced detection, stratification, and classification of cells: A review," *Biomed. Microdevices*, vol. 24, no. 3, p. 26, Aug. 2022.

Authorized licensed use limited to: Rutgers University Libraries. Downloaded on May 20,2025 at 20:38:08 UTC from IEEE Xplore. Restrictions apply.

[26] J. Mok, M. N. Mindrinos, R. W. Davis, and M. Javanmard, "Digital microfluidic assay for protein detection," *Proc. Nat. Acad. Sci.*, vol. 111, no. 6, pp. 2110–2115, Feb. 2014.

[27] M. Kokabi, J. Sui, N. Gandotra, A. P. Khamseh, C. Scharfe, and M. Javanmard, "Nucleic acid quantification by multi-frequency impedance cytometry and machine learning," *Biosensors*, vol. 13, no. 3, p. 316, Feb. 2023.

[28] Z. Lin et al., "Rapid assessment of surface markers on cancer cells using immuno-magnetic separation and multi-frequency impedance cytometry for targeted therapy," *Sci. Rep.*, vol. 10, no. 1, p. 3015, Feb. 2020.

[29] A. C. Gelijns and N. Rosenberg, "Diagnostic devices: An analysis of comparative advantages," in *Sources of Industrial Leadership*. Cambridge, U.K.: Cambridge Univ. Press, Jun. 2012, pp. 312–358.

[30] C. D. Chin, V. Linder, and S. K. Sia, "Commercialization of microfluidic point-of-care diagnostic devices," *Lab Chip*, vol. 12, no. 12, pp. 2118–2134, 2012.

[31] S. M. Alamouti, "A simple transmit diversity technique for wireless communications," *IEEE J. Sel. Areas Commun.*, vol. 16, no. 8, pp. 1451–1458, Oct. 1998.

[32] P. Xie, X. Cao, Z. Lin, N. Talukder, S. Emaminejad, and M. Javanmard, "Processing gain and noise in multi-electrode impedance cytometers: Comprehensive electrical design methodology and characterization," *Sens. Actuators B, Chem.*, vol. 241, pp. 672–680, Mar. 2017.

[33] T. Sun, C. van Berkel, N. G. Green, and H. Morgan, "Digital signal processing methods for impedance microfluidic cytometry," *Microfluidics Nanofluidics*, vol. 6, no. 2, pp. 179–187, Feb. 2009.

[34] D. Barat, D. Spencer, G. Benazzi, M. C. Mowlem, and H. Morgan, "Simultaneous high speed optical and impedance analysis of single particles with a microfluidic cytometer," *Lab Chip*, vol. 12, no. 1, pp. 118–126, 2012.

[35] J. Chen, C. Xue, Y. Zhao, D. Chen, M.-H. Wu, and J. Wang, "Microfluidic impedance flow cytometry enabling high-throughput single-cell electrical property characterization," *Int. J. Mol. Sci.*, vol. 16, no. 5, pp. 9804–9830, Apr. 2015.

[36] S. Joo, K. H. Kim, H. C. Kim, and T. D. Chung, "A portable microfluidic flow cytometer based on simultaneous detection of impedance and fluorescence," *Biosensors Bioelectron.*, vol. 25, no. 6, pp. 1509–1515, Feb. 2010.

[37] J. Sui, P. Xie, Z. Lin, and M. Javanmard, "Electronic classification of barcoded particles for multiplexed detection using supervised machine learning analysis," *Talanta*, vol. 215, Aug. 2020, Art. no. 120791.

[38] F. Caselli, R. Reale, A. De Ninno, D. Spencer, H. Morgan, and P. Bisegna, "Deciphering impedance cytometry signals with neural networks," *Lab Chip*, vol. 22, no. 9, pp. 1714–1722, 2022.

[39] A. A. Hutter, S. Mekrazi, B. N. Getu, and F. Platbrood, "Alamouti-based space-frequency coding for OFDM," *Wireless Pers. Commun.*, vol. 35, nos. 1–2, pp. 173–185, Oct. 2005.

[40] S. Atapattu and N. Rajatheva, "Analysis of Alamouti code transmission over TDMA-based cooperative protocol," in *Proc. Spring-IEEE Veh. Technol. Conf. (VTC)*, May 2008, pp. 1226–1230.

[41] J. H. Winters, "The diversity gain of transmit diversity in wireless systems with Rayleigh fading," *IEEE Trans. Veh. Technol.*, vol. 47, no. 1, pp. 119–123, Feb. 1998.

Authorized licensed use limited to: Rutgers University Libraries. Downloaded on May 20,2025 at 20:38:08 UTC from IEEE Xplore. Restrictions apply.